DISCOVERY OF ROTATIONAL MODULATIONS IN THE PLANETARY-MASS COMPANION 2M1207B: A SLOW ROTATION PERIOD AND CLOUD HEIGHT IN A LOW GRAVITY ATMOSPHERE

Yifan Zhou, Daniel Apai, Glenn Schneider
Steward Observatory, the University of Arizona

Mark Marley
NASA Ames Research Center
Draft version September 14, 2015

ABSTRACT

Rotational modulations of brown dwarfs have recently provided powerful constraints on the properties of ultra-cool atmospheres, including longitudinal and vertical cloud structures and cloud evolution. Furthermore, detection of periodic light curve variations can directly probe the rotational periods of ultra-cool objects.

We present here, for the first time, time-resolved high-precision photometric measurements of a planetary-mass companion, 2MASS1207b, to a brown dwarf primary. Using HST/WFC3 and point spread function combination with two spacecraft roll angles we detect photometric modulations in the light curve. The amplitude is 0.9% in the F160W and 1.5% in the F125W filters; we find a consistent period and similar phase in both bands. Joint fit to the light curve in both bands suggest a period of $10.2^{+0.9}_{-0.8}$ h. The relative amplitudes in the two filters are very similar to that found in a recent study of a field (high-gravity) L-dwarf, suggesting that the cloud structures that introduce the photometric modulations are similar in high- and low-gravity objects. Importantly, our study also measures, for the first time, the rotational period for directly imaged planetary-mass companion.

Subject headings: brown dwarfs – planets and satellites: atmospheres – planets and satellites: individual (2M1207b) – techniques: photometric

1. INTRODUCTION

Presence of condensate clouds is one the most unique and essential features of the ultra-cool atmosphere of direct imaged exoplanet and brown dwarfs. The formation and properties of condensate clouds of are intensively studied in recent years (e.g. Ackerman & Marley 2001; Helling et al. 2008; Allard et al. 2012), and great improvement has been achieved in understanding the cloud behavior across different spectral types, especially in the explanation of L-T transition (Marley et al. 2010). Surface gravity is suggested to be another key parameters in defining cloud structures. Low surface gravity objects (e.g. HR8799 bcd, 2M1207 b) have significantly redder color compared to their spectral type matched brown dwarfs, which are best explained by the existence of thick clouds (Barman et al. 2011; Skemer et al. 2011, 2012). However, due to lack of observational constraint, the behavior of clouds in the atmospheres of low surface gravity objects are not as well as modeled as high surface gravity counterpart.

Intensity modulations introduced by heterogeneous clouds can be directly observed and studied via time resolved observation and rotational mapping. These techniques isolate the effect of cloud properties and obtained great success in determining the rotation period and unveiling the structures of the atmosphere of brown dwarfs (e.g. Apai et al. 2013; Buenzli et al. 2012, 2015; Burgasser et al. 2013; Radigan et al. 2012; Yang et al. 2014; Metchev et al. 2015). Kostov & Apai (2013) demonstrated the great potential of these techniques in the study of the cloud properties of direct imaged exoplanets and plan-

etary mass companions. However, high brightness contrast makes it much more challenging for direct imaged exoplanet and planetary mass companions than brown dwarfs to acquire high-precision light curves.

2M1207 b (Chauvin et al. 2005) is a planetary mass companion that has mass of $\sim 4M_{\rm Jup}$ and an angular separation of $0.78''$ to its host 2M1207 A, an M8 brown dwarf. Relative moderate contrast (6.7 mag in J band, Mohanty et al. (2007)) makes it one the most feasible planetary mass companions for high-precision time-resolved observation and the best starting points for developing strategies for time-resolved observation and data reduction in high contrast case.

In this *Letter* we present the first, high-cadence, high-precision, time-resolved *Hubble Space Telescope* (HST) photometric time series of 2M1207 b, a directly imaged planet or planetary-mass object. We successfully detect rotational modulation and measure the amplitudes in two bands and determine the rotational period.

2. OBSERVATION

We obtained direct images of the 2M1207A+b system on UT 2014 April 11from 08:07:47 to 16:53:18 using HST and its Wide Field Camera 3 (WFC3, Kimble et al. 2008) in the frame of the HST Proposal GO-13418 (PI: D. Apai). We acquired the observations in filters F125W ($\lambda_{\rm pivot}$ = 1245.9 nm, full width at half maximum (FWHM) = 301.5 nm) and F160W ($\lambda_{\rm pivot}$ 1540.52, FWHM = 287.9 nm), roughly corresponding to the J and H bands. The WFC3 pixel scale is ≈13mas. We used the 256×256 pixels sub-array mode to avoid mem-
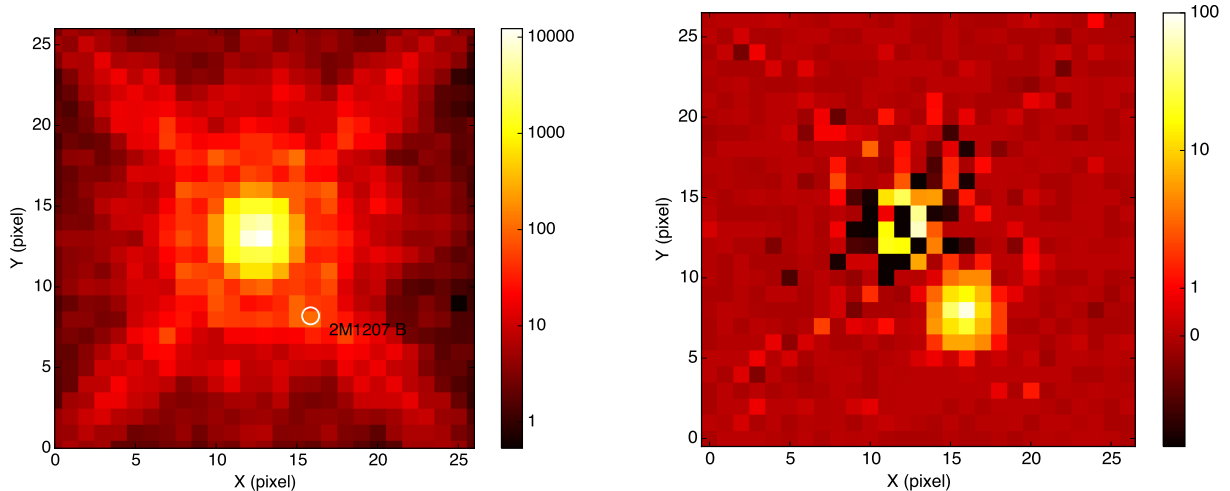
FIG. 1.— WFC3 F160W images for 2M1207 system. *Upper panel*: original image, the position of 2M1207b is indicated using white circle. *Lower panel:* residual image – after the subtraction of the hybrid PSF, 2M1207 B is detected at a high significant level.

ory dumps during the observations. In order to provide a near-continuous coverage for detecting modulations we observed the 2M1207 system in six consecutive HST orbits, obtaining data with cadence of $\sim$ 1.5 minutes over a baseline of 8 hours and 40 minutes. The observations were interrupted by 58 minutes long Earth occultations every 94 minutes.

The observations applied space craft rolls between each two orbits to allow roll-subtraction of the primary (e.g. Song et al. 2006). The telescope roll angles for orbits 1, 3, and 5, and those taken in orbits 2, 4, and 6 differed by 25°. At the separation of 2M1207b this angle difference corresponds to a displacement of 0.34″ or 2.75 and 2.30 resolution elements in F125W and F160W, respectively. In each orbit we took thirteen SPARS10 non-destructive read-outs with NSAMP=10, alternating between F160W and F125W filters, with 2–3 identical exposures in one exposure sequence. To improve sampling and reduce the risk that point spread funciton (PSF) lays on bad pixels, we applied a 4-point dither pattern with differential "X/Y" offsets of 1.375" in the detector frame, providing optimal non-integral (half pixel) stepping of 10.5 and 8.5 pixels in F125W and F160W, respectively. Over the 6 orbits, we obtained 70 images with 10 non-destructive read-outs in F125W and 64 images in F160W with exposure time of 88.4 s in each filters.

3. DATA REDUCTION

3.1. *Photometry*

We started the reduction from the the `flt` files files produced by the WFC3's `calwfc3` pipeline. We did not opt to use the more advance `ima` files pipeline products because these provided less information on 2M1207A, which saturated after the first few read-outs. The `flt` files are results of basic calibration, including dark current correction, non-linearity correction, flat field correction, as well as up-the-ramp fit on the non-destructive read-outs also considering cosmic rays. From the beginning, pixels with data quality flags "bad detector pixels", "unstable response", and "bad or uncertain flat value" were masked out and excluded from further analysis as suggested by previous transit exoplanet spectroscopic ob-

servations(e.g. Berta et al. 2012; Kreidberg et al. 2014).

One major challenge of high contrast imaging observation using WFC3/IR is significant under-sampling of the detector. 2M1207 A and b are only separated by $\sim$ 6 pixels or $\sim$5 FWHM of the PSF. When applying roll subtraction, notable artifact structures are generated by image interpolation and shifting. On the other hand, *Tiny Tim* PSF simulator(Krist 1995) offers a solution by providing Nyquist or better sampled PSF, but systematic errors of *Tiny Tim* PSF for WFC3 limits its ability in high precision photometry(Biretta 2014). However, we are able to fully characterize the difference of model and observed PSFs with 6 orbits time-resolved observation data. To obtain robust *Tiny Tim* PSF photometry, we designed a 2-round PSF fitting strategy: 1. calculating correction map for *Tiny Tim*; 2. hybrid PSF photometry.

For both of 2 rounds, we used *Tiny Tim* to calculate 10× over-sampled model PSFs based on the filters, the spectra (Bonnefoy et al. 2014; Patience et al. 2010), the telescope's actual focus, and the telescope jitter. We used the new set of Tiny Tim parameters provided by Biretta (2014) to improve model of the cold mask, OTA spikes, and the coma. The focus parameters were calculated using the model listed on the STScI website[1]. To register *Tiny Tim* PSF to observed PSF of 2M1207A, we moved the over-sampled PSF over a coordinate grid (gird size=0.001 pixel) using cubic interpolation and minimize the rms difference of the observed and re-binned *Tiny Tim* PSFs over a region centered on 2M1207A with a 5-pixel-radius aperture centered on 2M1207b excluded. Then we introduce another *Tiny Tim* PSF for 2M1207b and fit the position of 2M1207 b and the photometries of 2M1207 A and b simultaneously by least square optimization. From our data set, we discovered that the difference of observed PSFs and model PSFs were very stable for given PSF positions. Therefore, at the end of the first round PSF fitting, we derived 8 (2 roll angles × 4 dithering positions) observationally derived correction

---

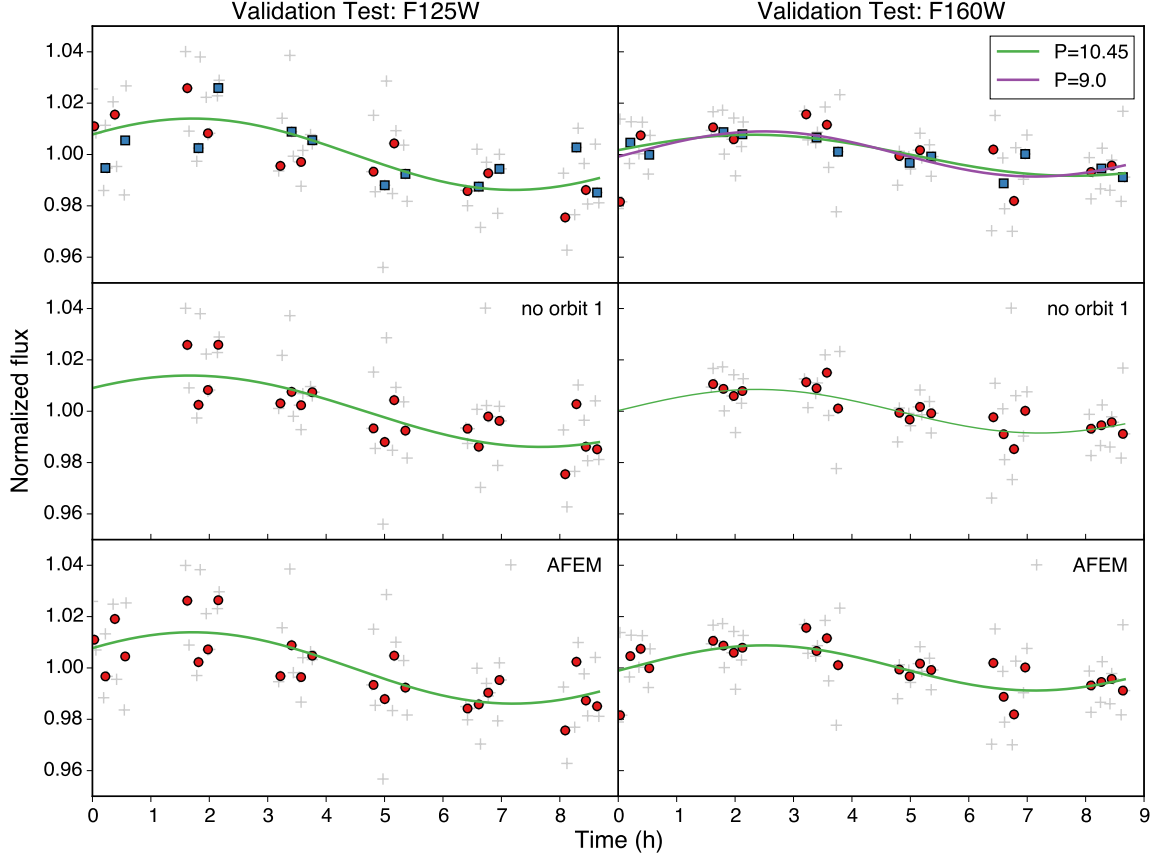[1] http://www.stsci.edu/hst/observatory/focus/FocusModel

FIG. 2.— F125W (left) and F160W (right) light curves under different variability verification tests. Individual measurements are plotted with gray crosses. Photometric measurements of the same exposure sequence are binned, and binned photometry are plotted with points or squares. Best fitted sinusoidal curves are plotted with solid lines. *Upper*: binned measurements taken in dithering position 1 and 3 (red points) and that taken in 2 and 4 (blue squares) are plotted with different symbols. They demonstrate same trend of variation. In upper left panel, green line is sinusoidal wave fitted with all parameter set free, and purple line is sinusoidal wave fitted with period set the same as that of F125W. *Middle*: sinusoidal waves fitted without using the data taken in Orbit #1. These curves are almost identical to the curves plotted in upper panel. *Lower*: photometry measured with AFEM-added images and best fitted sinusoidal curves. These points and curves are also almost identical to those plotted in the upper panel.

maps for each filter:

$$\text{Corr} = \text{Median}(\text{PSF}_{\text{obs.}} - \text{PSF}_{\text{model}}) \qquad (1)$$

where $\text{PSF}_{\text{model}}$ is a combination of two *Tiny Tim* PSFs for 2M1207 A and b. In the second round, we combined the correction term linearly with the two *Tiny Tim* PSFs to generate hybrid PSFs, and fitted the three components together. We found that by including the correction term, the reduced χ^2 of PSF fitting is decreased from ~ 10 to around unity. Relative photometry is acquired from the scaling parameters of the model PSFs.

PSF profiles change with exposure positions due to pixelation, especially for the case that WFC3 IR is significantly under-sampled. Also, the flat fields may potentially have large scale structures (Dressel 2012). We found a correlation of photometry with PSF positions on detector frame for both 2M1207 A and b. Correction were made by normalizing each group of exposures that have the same dithering position and roll angle individually – we took the median of the fluxes that were measured from these exposures as normalization factors and divided them from every photometric measurement. Because the normalization factor for each group of exposures is calculated across the whole observation, this normalization step has negligible impacts on variability

analysis.

3.2. *Uncertainty Analysis: White noise*

First we estimated the photon noises for the photometry of 2M1207b. We propagated the photon noises of every single pixel that were calculated from count rates and detector gain, to the PSF fitting results. The photon noises for photometry in F125W and F160W are 1.33% and 1.02%, respectively.

Since the PSFs for the 2M1207 A and b were fitted simultaneously in the PSF photometry procedure, the uncertainties of photometry and position for the primary and secondary are coupled. Imperfection of position measurement of 2M1207A could potentially affect the photometry of 2M1207b. We used a Monte Carlo (MC) method to evaluate the overall systematic of the PSF fitting. We applied the PSF photometry to images that were added with random Poisson noises and repeat the photometry procedure for 1000 times. From the distribution of the result, the uncertainty for F125W and F160W photometry are 1.34% and 1.12%, respectively. We conclude that the white noise of our observation is dominated by photon noise.

3.3. *Uncertainty Analysis: Flat field uncertainties*

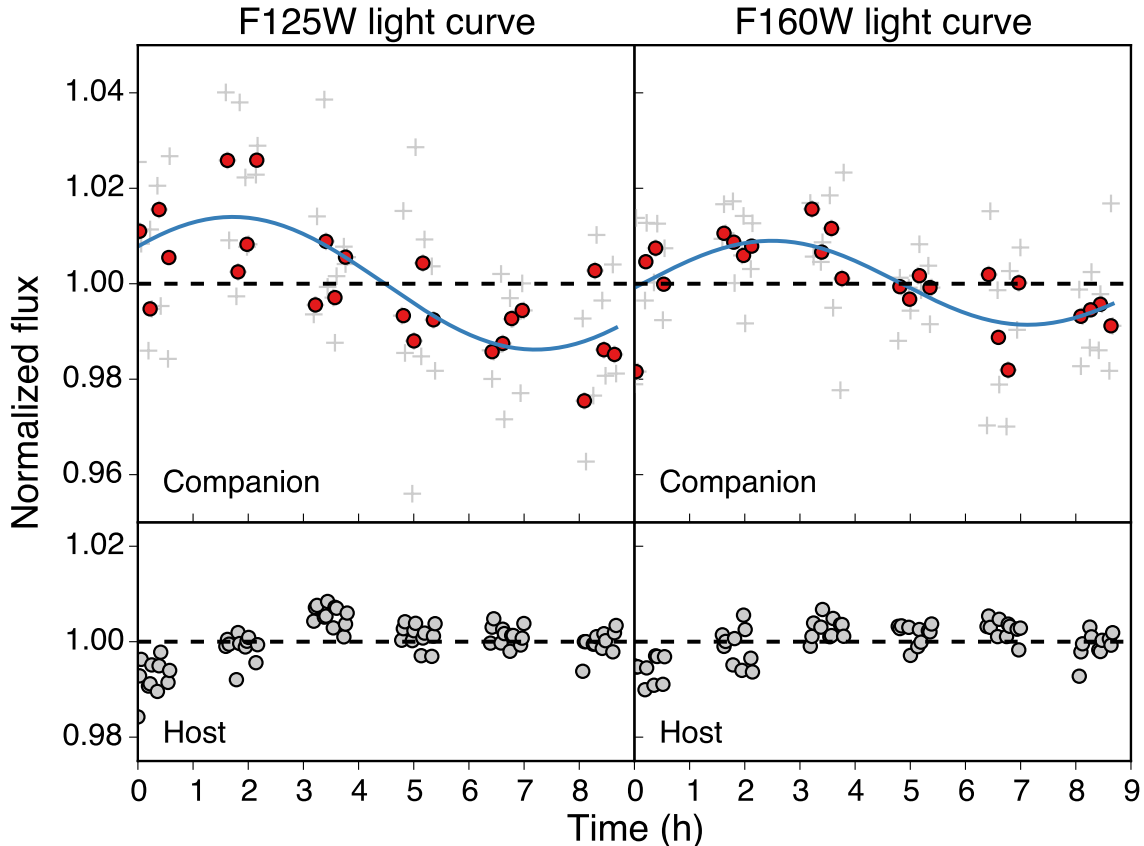## F125W light curve   F160W light curve

FIG. 3.— Normalized light curves for 2M1207 B (upper) and A (lower) with filter F125W (left) and F160W (right). Individual photometric measurement are plotted in gray crosses and binned photometry are plotted with red points. Best fitted sinusoidal waves are plotted with blue solid lines.

2M1207b were observed at 8 different spots on the detector (2 rolls × 4 dithering positions). Imperfect flat field correction are potential sources of variation as they may introduce position-dependent differences in the count rates. The uncertainty of WFC3 IR pipeline flat field is typically ∼ 1% (Dressel 2012).

In PSF photometry, however, multiple pixels are fitted simultaneously and we expect a lower than 1% uncertainty from the flat field errors. To verify this, we multiplied every image by an artificial flat field error mask (AFEM) – a uniformly distributed Gaussian noise array with mean of 1 and sigma of 1% – and repeated the PSF photometry on the resulting images. The analysis of these experiments showed almost identical light curve to the original, verifying that the flat field errors do not affect our photometry significantly (Figure 2).

4. VERIFICATION OF PHOTOMETRIC VARIATIONS AND AMPLITUDE ESTIMATE

4.1. *Tests and Verification*

The light curves that resulted from our photometry show apparently sinusoidal modulations, discussed in more details in §5. To verify that these modulations are intrinsic to the object and not result of our data reduction procedure or due to instrumental changes, we carried out three different tests.

First, we fitted sine waves independently to the two filters to verify the similarity of the signal in the two bands (Figure 2). Inconsistent periods or light curve shapes

would argue against a genuine signal. We found that the periods of the best fit sine waves are similar, $10.5^{+1.2}_{-1.3}$h for F125W and $9.1^{+1.1}_{-1.0}$h for F160W. These periods are roughly consistent within the uncertainty. Furthermore, these periods are not close to any timescales over which HST or WFC3 are known to changes.

As a second test we repeated the analysis neglecting the first orbit. The motivation behind this test was that, due to spacecraft thermal settling, the first orbit of HST observations is often slightly unstable and is often neglected in high-precision studies (**citation?**). Indeed, in our analysis 2M1207 A is significantly fainter in the first orbit (Figure 3) than in the subsequent ones. Our analysis based on orbits 2–6 only found essentially identical results to our analysis of orbits 1–6, based on which we conclude that the first less reliable orbit does not affect our results significantly (Figure 2, middle panel).

As a third test we explored whether a subset of images, perhaps imperfectly normalized or correlated with specific instrument states, could be driving the light curves into an apparently sinusoidal shape. To test this possibility we split the data into two temporally overlapping halves: sub-dataset one from dithering positions 1 and 3, and sub-dataset two from dithering positions 2 and 4. For both datasets we repeated our analysis independently. For both of F125W and F160W, two halves demonstrated similar trend of variability as shown in Figure 2. Our analysis detected sinusoidal modulations in
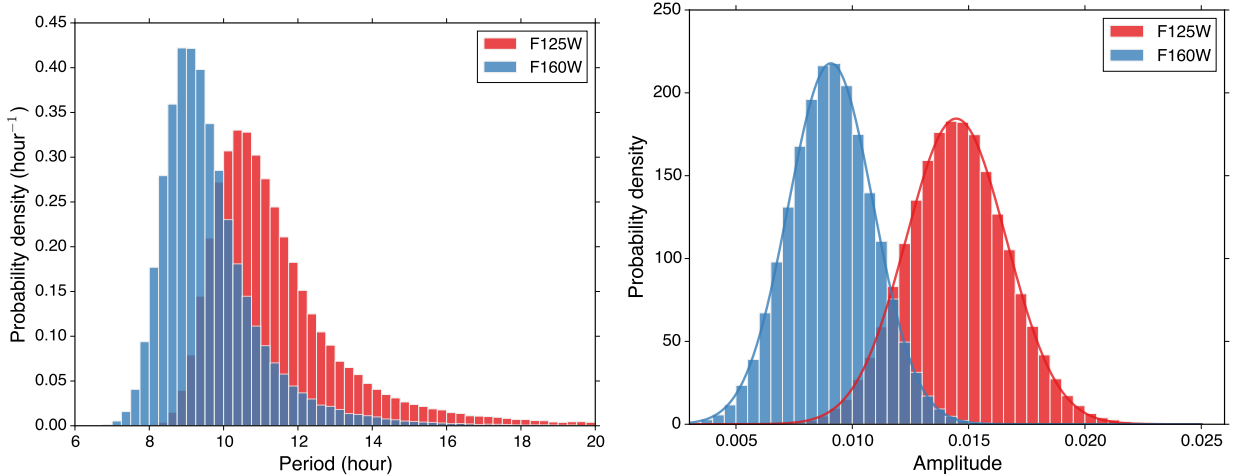
FIG. 4.— Distributions for periods (left) and amplitudes(right) for the light curve of F125W and F160W. The bin size for histograms of period is 0.25 hour and for that of amplitude is 0.5%. Histograms are normalized in the way that total area of the histogram equals to 1. In the right panel, Gaussian profiles are fitted to the histograms of periods and plotted in solid lines.

both sub-datasets and in *both* filters, with periods and amplitudes consistent with those derived from the complete data set (2, upper panel).

These tests demonstrate that the modulation seen in our data are consistently present in the different filters, in the different time segments of the data, and in data obtained in different dithering positions.

4.2. Amplitude and Period Measurements

To constrain the uncertainties of the least square optimization results, we used a MC method to improve the fitting. We generated a series of random Gaussian noises with the standard deviation same as the photon noise, added them to the original light curves, and applied least square fit to the new light curves. We repeated above routine for 100,000 times and obtained the distribution of the fitting parameters. The distributions for the periods and the amplitudes for F125W and F160W light curves are shown in Figure 4.

5. RESULT

We present the first high-resolution, high-cadence, and high-precision photometry of a directly imaged planet or planetary-mass companion. Our observations reveal a modulation in the light curve of the $\sim 4 M_{\rm Jup}$ companion 2M1207b, the first detection of modulations in directly imaged planetary mass objects. The best fit periods for F125W and F160W are 10.5 and 9.1 hour correspondingly. The amplitudes for the normalized light curves are 1.45% and 0.92% for F125W and F160W light curves.

We obtained high signal to noise photometry series for both 2M1207 A and B (Figure 3). On average, the photometric contrast is 6.52 ± 0.01 mag for F125W and 5.77 ± 0.01 mag for F160W. The difference of F125W contrast from that measured in J-band (Mohanty et al. 2007) and F160W contrast from that measured with NICMOS F160W (Song et al. 2006) is due to the different throughput profiles of the filters.

The distributions for the periods demonstrate long tail shaped towards long period, with core region roughly Gaussian. With 64% confidence, we estimated the 1-σ range for the periods of F125W and F160W to be

$10.5^{+1.3}_{-1.2}$ and $9.1^{+1.1}_{-1.0}$ h, respectively. The period of best fitted sine wave of F125W light curve is 1.5h longer than that of F160W, and 0.3–0.4 h larger 1-σ standard deviation. We also jointly fit the two band light curves together forcing the periods of two sinusoids to be the same. We derived a modulation period of $10.2^{+0.9}_{-0.8}$ h.

We discover that the variation amplitudes in the two bands are significantly different. By fitting Gaussians to the MC fit result distributions, we determined that variation amplitude of F125W is 1.45% with a standard deviation of 0.22%, and that of F160W is 0.92% with a standard deviation of 0.20%. The peaks of the two histograms separate by more than 2-σ. The variation amplitude for F125W is 1.58 times of that of F160W light curve.

6. DISCUSSION

A fundamental result of our study is the direct determination of the rotation period of a directly imaged planetary mass object. In the left panel of Figure 5 we compare the rotation period of 2M1207b to the solar system planets, β Picb the only other directly imaged planet with an estimated period and measured $v \sin i$, and field brown dwarfs from the study of (Metchev et al. 2015). The study by (Snellen et al. 2014) succeeded in measuring $v \sin i$ for β Picb and demonstrated that it fits a trend defined by Solar System planets in which more massive planets have faster rotation rates. The interesting finding that β Picb, an exoplanet that formed in a protoplanetary disk, follows this trend suggests a possibly connection between planet mass, initial angular momentum, and formation in a disk.

Excitingly, our measurement of the rotation period of 2M1207b, a planet mass companion that has similar age to β Picb, has a rotation period that fits in the same trend, as well as majority of brown dwarfs. We note that 2M1207 b is most likely formed in the same way as brown dwarfs by gravitational fragmentation. The result that objects formed in different scenarios share the same trend of period vs. mass suggests that rotation periods – in absence of well-determined ages – are not good tracers of the formation pathways and may not contribute
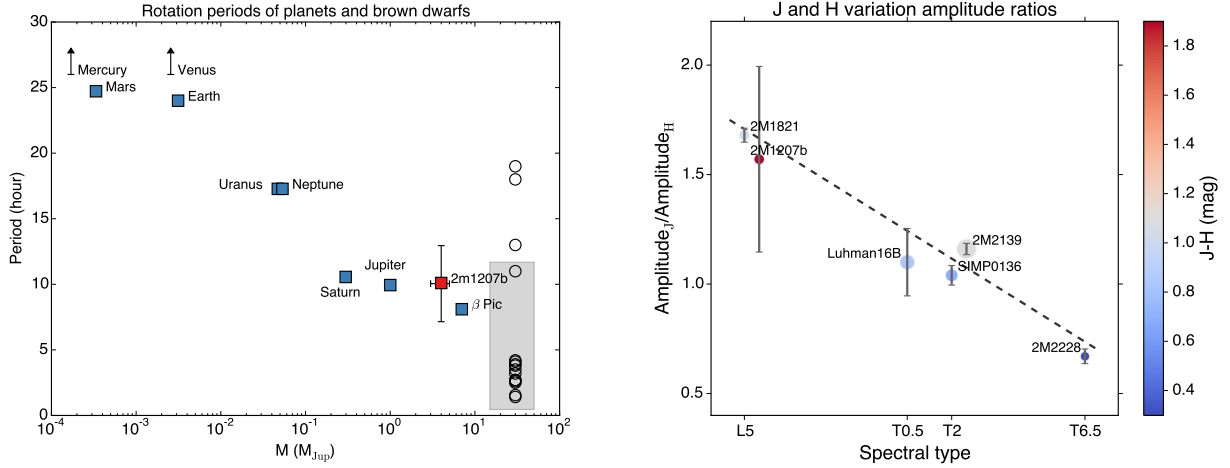
FIG. 5.— comparison of 2M1207's rotation period and color change with brown dwarfs, β Pic b, and solar system planets. *Left*: period vs. mass plot for 2M1207b (red square), solar system planets and β Pic b (blue squares), and brown dwarfs (black circles, gray shade). The mass of brown dwarfs are assumed to be 30 $M_{\rm Jup}$. The gray rectangle that has a ±15 $M_{\rm Jup}$ range in x, and a $\pm\sigma$ of brown dwarf periods range in y, indicates a region where brown dwarfs most likely to appear in this diagram. Rotation period monotonically decreases with the increase of mass. *Right*: ratio of variation amplitude in J and H band vs. spectral type for 2M1207b and brown dwarfs. The colors of the points represent J−H magnitude, and the sizes of the points are proportional to the J band variation amplitudes. The gray dashed line is the result of a linear fit to these points. Tight linear correlation of J- and H-band variation ratio and spectral type is demonstrated in this diagram.

x

important evidence for a formation in a disk vs. in a cloud core environment. *Add younger BDs and this may change*

Furthermore, our observations allow us to compare the relative amplitudes in the J- and H-bands with the handful of brown dwarfs for which high-quality near-infrared time-resolved observations have been obtained. In the right panel of Figure 5, we compare the relative amplitude of J- and H-bands of 2M1207b and brown dwarfs (Apai et al. 2013; Buenzli et al. 2012, 2015; Burgasser et al. 2013; Radigan et al. 2012; Yang et al. 2014) that have different spectral types and J−H colors.

We find a tight correlation between the spectral type of the object and the J- to H-band variation amplitude ratio. In the right panel of Figure 5, we demonstrate that earlier spectral type objects, independent of their surface gravity, have larger variations at shorter wavelength than at longer wavelengths. Importantly, although the J−H color of 2M1207b is significantly redder, its relative variation amplitude ratio is almost identical to the matching spectral type mid-L dwarf 2M1821.

This trend can be qualitatively explained using the toy model proposed in Yang et al. (2014) within the spectral type range of mid-L to L-T transition. Assuming that intensity modulations are introduced by a refractory cloud whose upper layer locates at altitude z, the variation amplitude ratio for J and H band can be expressed as $\mathrm{Amp_J/Amp_H} = \exp\left[-(\tau_J(z)/\tau_H(z))\right]$, where $\tau_J(z)$ and $\tau_H(z)$ are the optical depths of upper cloud layer for J and H bands. The opacity for J band is smaller than that for H, therefore from mid-L to L-T transition, as the cloud upper boundary appears higher in the atmosphere, the optical depth difference for the two bands gets smaller, and the amplitude ratio decreases. We note,

that the late T dwarf 2M2228 falls exactly on this trend, but whose variations are likely to emerge from a different mechanism as their silicate clouds are below the visible photosphere (e.g. Stephens et al. 2009).

We infer that the upper cloud layer of 2M1207b is at a similar optical depth as that of a matching spectral type field brown dwarf from the fact that they share similar J- and H-bands light curve amplitude ratio.

7. CONCLUSIONS

In summary, from our J- and H-band high precision, high-cadence light curves we discovered sinusoidal modulations in the planetary mass object 2M1207b. This is the first detection of rotational modulations in a directly imaged planetary mass object. The period is $10.2^{+0.9}_{-0.8}$, similar to that derived from $v\sin i$ measurements for the direct imaged exoplanet β Pic b and significantly longer than most field brown dwarfs with known rotation periods. The modulation amplitude ratio of J and H band is almost identical to one matching spectral type L5 dwarf, although they have very different J−H colors.

Finally, we note that the observations presented here open an exciting new window on directly imaged exoplanets and planetary-mass companions. Our study demonstrates a successful application of high-cadence, high-precision, high-contrast photometry with planetary mass companion. We also show that these observations can be carried out simultaneously at multiple wavelengths, allowing us to prove multiple pressure levels. With observation of a larger sample and at multiple wavelengths, we will be able to explore the detailed structures of atmospheres of directly imaged exoplanets, and identify the key parameters that determine these.

REFERENCES

Ackerman, A. S. & Marley, M. S. 2001, ApJ, 556, 872
Allard, F., Homeier, D., & Freytag, B. 2012, Royal Society of London Philosophical Transactions Series A, 370, 2765

Apai, D., Radigan, J., Buenzli, E., Burrows, A., Reid, I. N., & Jayawardhana, R. 2013, ApJ, 768, 121

Barman, T. S., Macintosh, B., Konopacky, Q. M., & Marois, C. 2011, ApJ, 733, 65

Berta, Z. K., Charbonneau, D., Désert, J.-M., et al. 2012, ApJ, 747, 35

Biretta, J. 2014, Space Telescope WFC Instrument Science Report, 1, 10

Bonnefoy, M., Chauvin, G., Lagrange, A.-M., Rojo, P., Allard, F., Pinte, C., Dumas, C., & Homeier, D. 2014, A&A, 562, A127

Buenzli, E., Apai, D., Morley, C. V., Flateau, D., Showman, A. P., Burrows, A., Marley, M. S., Lewis, N. K., & Reid, I. N. 2012, ApJ, 760, L31

Buenzli, E., Saumon, D., Marley, M. S., Apai, D., Radigan, J., Bedin, L. R., Reid, I. N., & Morley, C. V. 2015, ApJ, 798, 127

Burgasser, A. J., Sheppard, S. S., & Luhman, K. L. 2013, ApJ, 772, 129

Chauvin, G., Lagrange, A.-M., Dumas, C., Zuckerman, B., Mouillet, D., Song, I., Beuzit, J.-L., & Lowrance, P. 2005, A&A, 438, L25

Dressel, L. 2012, Wide Field Camera 3, HST Instrument Handbook, 1

Helling, C., Ackerman, A., Allard, F., Dehn, M., Hauschildt, P., Homeier, D., Lodders, K., Marley, M., Rietmeijer, F., Tsuji, T., & Woitke, P. 2008, MNRAS, 391, 1854

Kimble, R. A., MacKenty, J. W., O'Connell, R. W., & Townsend, J. A. 2008, in Society of Photo-Optical Instrumentation Engineers (SPIE) Conference Series, Vol. 7010, Society of Photo-Optical Instrumentation Engineers (SPIE) Conference Series, 1

Kostov, V. & Apai, D. 2013, ApJ, 762, 47

Kreidberg, L., Bean, J. L., Désert, J.-M., et al. 2014, Nature, 505, 69

Krist, J. 1995, in Astronomical Data Analysis Software and Systems IV, Vol. 77, 349

Marley, M. S., Saumon, D., & Goldblatt, C. 2010, ApJ, 723, L117

Metchev, S. A., Heinze, A., Apai, D., Flateau, D., Radigan, J., Burgasser, A., Marley, M. S., Artigau, E., Plavchan, P., & Goldman, B. 2015, ApJ, 799, 154

Mohanty, S., Jayawardhana, R., Huelamo, N., & Mamajek, E. 2007, ApJ, 657, 1064

Patience, J., King, R. R., De Rosa, R. J., & Marois, C. 2010, A&A, 517, A76

Radigan, J., Jayawardhana, R., Lafrenière, D., Artigau, E., Marley, M., & Saumon, D. 2012, ApJ, 750, 105

Skemer, A. J., Close, L. M., Szűcs, L., Apai, D., Pascucci, I., & Biller, B. A. 2011, ApJ, 732, 107

Skemer, A. J., Hinz, P. M., Esposito, S., Burrows, A., et al. 2012, ApJ, 753, 14

Snellen, I. A. G., Brandl, B. R., de Kok, R. J., Brogi, M., Birkby, J., & Schwarz, H. 2014, Nature, 509, 63

Song, I., Schneider, G., Zuckerman, B., Farihi, J., Becklin, E. E., Bessell, M. S., Lowrance, P., & Macintosh, B. A. 2006, ApJ, 652, 724

Stephens, D. C., Leggett, S. K., Cushing, M. C., Marley, M. S., Saumon, D., Geballe, T. R., Golimowski, D. A., Fan, X., & Noll, K. S. 2009, ApJ, 702, 154

Yang, H., Apai, D., Marley, M. S., Saumon, D., Morley, C. V., Buenzli, E., Artigau, E., Radigan, J., Metchev, S., Burgasser, A. J., Mohanty, S., Lowrance, P. J., Showman, A. P., Karalidi, T., Flateau, D., & Heinze, A. N. 2014, ApJ, 798, L13